Electronic Supplementary Material (ESI) for Soft Matter.

Supporting information

Role of Confinement on the Shear Banding and Shear Jamming in Noncolloidal Fiber Suspensions

Benke Li[1, 2], Wei You[1], Sijun Liu[1], Li Peng[2], Xianbo Huang[2]*, Wei Yu[1]*

1. *Advanced Rheology Institute, State Key Laboratory for Metal Matrix Composite Materials, Department of Polymer Science and Engineering, Shanghai Key Laboratory of Electrical Insulation and Thermal Ageing, Department of Polymer Science and Engineering, Shanghai Jiao Tong University, Shanghai 200240, P.R. China*
2. *National-certified Enterprise Technology Center, Kingfa Science and Technology Co., LTD., Guangzhou 510663, P. R. China*

1. Settlement Effect

The GF settlement effect in the PEB matrix can be estimated by solving the force equilibrium equation between the gravity and the hydrodynamic drag force: $\mathbf{F}_{\text{gravity}} = \zeta_{\parallel}\mathbf{pp}\cdot\mathbf{V}_{\text{settle}} + \zeta_{\perp}(\mathbf{I}-\mathbf{pp})\cdot\mathbf{V}_{\text{settle}}$ [1]. $\mathbf{p}$ is the unit orientational vector of the fiber, $\left\|\mathbf{F}_{\text{gravity}}\right\| = \frac{\pi d^2}{4}L(\rho_{GF}-\rho_{PEB})g$, and $\zeta_{\parallel}$, $\zeta_{\perp}$ are the parallel and perpendicular components of the translational friction constant, respectively. The friction constants have been given by Kirkwood [1] as: $\zeta_{\parallel} = 2\pi\eta_s L/\ln(L/d)$ and $\zeta_{\perp} = 2\zeta_{\parallel}$. So we get the velocity of the settlement of the glass fibers: $\|\mathbf{V}_{\text{settle}}\| \le \left\|\mathbf{F}_{\text{gravity}}\right\|/\zeta_{\perp} = 2.7\times10^{-3}$ μm/s (using $\eta_s = 330$ Pa·s, $L = 219$ μm, $d = 18.4$ μm, $\rho_{GF} = 2.5$ g/cm^3, $\rho_{PEB} = 0.893$ g/cm^3). The time that a GF settles down to a distance of fiber diameter is $t_{\text{settle}} = d/v \ge 7000$ s, which is much longer than our experimental time scales. During our experiments, we did not observe the fiber settlements even when the PEB/GF samples were left still for two days under experimental temperature (160 °C). Thus, the GF settlement effect in the PEB matrix is negligible.

2. Stiffness of Fibers

Whether the GF is rigid could be judged from the applied shear stress σ_{shear} and the critical stress σ_{buck} at which the GF is expected to buckle under compression in the shear. The effective stiffness S^{eff} of the fibers can be characterized by the ratio between two stresses [2-4]:

$$S^{\text{eff}} = \frac{\sigma_{\text{buck}}}{\sigma_{\text{shear}}} \approx 1.2\frac{E\ln(2a_r)}{a_r^4\sigma_{\text{shear}}} \qquad \text{(S1)}$$

where E is the fibers' Young modulus (E ≈ 7.4 GPa for GF). For the typical shear stress in our experiments $\sigma_{\text{shear}} = 100$ Pa, the effective stiffness S^{eff} is about 14,478. Such a large value of S^{eff} guarantees the glass fibers behave rigid-like in the experiments. In our experiments, the bending of GF is not observed.

3. Apparent Rheology Using Cone-Plate

To compare with the parallel plates results, we made our sample into donut shape

(inner radius of 20 mm and outer radius of 30 mm) and put them into the cone-plate geometries (30 mm diameter with a cone angle of 0.1rad) to reduce the shear gradient effects in the radical direction. The results are shown in Fig. S1, which was consistent with the results in parallel plates (Fig. 3).

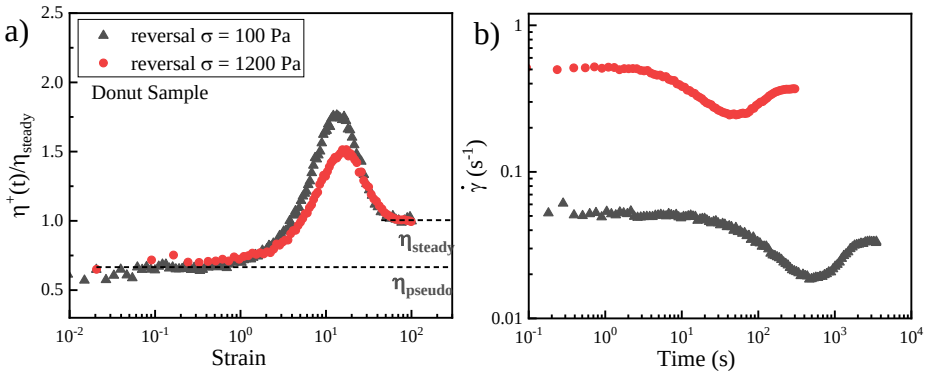

Figure S1. (a) Plots of normalized transient shear viscosity $\eta^+(t)/\eta_{\mathrm{steady}}$ during the reversal shear of donut-shaped samples, the inner diameter of the sample is 20 mm, and the outer diameter of the samples is 30 mm, the geometry was chosen as cone-plate geometries (30 mm diameter with a cone angle of 0.1rad). The shear stresses are 100 Pa and 1200 Pa, respectively. (b) The corresponding plots of shear rate versus time.

4. Introduction of FT Model

The state of rigid fiber alignment can be quantified by the orientation probability distribution function $\psi(\mathbf{p})$ with the unit vector $\mathbf{p}$ representing the orientation of a single fiber. The orientation tensor $\mathbf{A}$ is defined as the averaged dyadic product of $\mathbf{p}$ over the orientation space, $\mathbf{A} = \oint \psi(\mathbf{p})\mathbf{pp}d\mathbf{p}$ [5]. Higher-order orientation tensor can be defined similarly, for example, the fourth-order orientation tensor $\mathbf{A}_4$ is defined as $\mathbf{A_4} = \oint \psi(\mathbf{p})\mathbf{pppp}d\mathbf{p}$. The orientation tensor $\mathbf{A}_4$ will appear in the evolution equation of the orientation tensor $\mathbf{A}$, which means a closure is necessary. The invariant-based optimal fitting (IBOF) closure [6] or the orthotropic fitted closure [7] are two frequently used methods in the calculation.

In the dilute region, Jeffery [8] proposed a model for the rotational motion of the ellipsoid-like fibers, where only the hydrodynamic force was considered, and the interactions between the fibers were ignored. According to Jeffery model, the evolution

of single fiber orientation is described by:

$$\dot{\mathbf{p}}^{\mathrm{HD}} = \mathbf{W}\cdot\mathbf{p} + \xi(\mathbf{D}\cdot\mathbf{p} - \mathbf{D}\colon\mathbf{ppp}) \tag{S2}$$

where $\mathbf{W} = \frac{1}{2}(\boldsymbol{\nabla}\mathbf{v} - \boldsymbol{\nabla}\mathbf{v}^{\mathrm{T}})$, $\mathbf{D} = \frac{1}{2}(\boldsymbol{\nabla}\mathbf{v} + \boldsymbol{\nabla}\mathbf{v}^{\mathrm{T}})$, $\xi = \left(a_r^{*2} - 1\right)/\left(a_r^{*2} + 1\right)$ and a_r^* is the effective aspect ratio of the cylindrical fibers. a_r^* could be obtained by Zhang and Smith model [9] as $a_r^* = 0.000035\,a_r^3 - 0.00467\,a_r^2 + 0.764\,a_r + 0.404$, where a_r is the geometry aspect ratio of the fibers. Jeffery model can be reformulated using the second-order orientation tensor as:

$$\dot{\mathbf{A}}^{\mathrm{HD}} = (\mathbf{W}\cdot\mathbf{A} - \mathbf{A}\cdot\mathbf{W}) + \xi(\mathbf{D}\cdot\mathbf{A} + \mathbf{A}\cdot\mathbf{D} - 2\mathbf{A_4}\colon\mathbf{D}) \tag{S3}$$

In the semi-dilute region, the interaction between the fibers was considered by Folgar and Tucker [10] by introducing an isotropic rotational diffusion term:

$$\dot{\mathbf{A}} = (\mathbf{W}\cdot\mathbf{A} - \mathbf{A}\cdot\mathbf{W}) + \xi(\mathbf{D}\cdot\mathbf{A} + \mathbf{A}\cdot\mathbf{D} - 2\mathbf{A_4}\colon\mathbf{D}) + 2C_I|\dot{\gamma}|(\mathbf{I} - 3\mathbf{A}) \tag{S4}$$

where $\mathbf{I}$ is the unit tensor, C_I represents the diffusion coefficient of the fibers due to the collision of fibers, $\dot{\gamma}$ is the flow shear rate. Based on calculations of the diffusion coefficient using a direct simulation of the fiber dynamics, Phan-Thien et al. [11] proposed that C_I is related with the fiber volume content φ using the following equation

$$C_I = 0.03\,[1 - \exp(-0.224\,a_r\varphi)] \tag{S5}$$

which is also consistent with the experimental results by Folgar and Tucker [10]. C_I was strongly influencd by the confinement effect. And the C_I value under unconfinement condition C_I^{∞} was proposed by Benke Li et. al. [12] based on the Image Analysis method and PTV (Particle Tracking Velocity) method:

$$C_I^{\infty} = 0.0345\,[1 - \exp(-0.483 a_r\varphi)] \tag{S6}$$

5. Effect of Brownian Motion

The influence of rest time on the fiber orientation could be estimated by including the Brownian term in the FT model, as follows.

$$\dot{\mathbf{A}} = \dot{\mathbf{A}}^{\mathrm{J}} + \dot{\mathbf{A}}^{\mathrm{FT}} + \dot{\mathbf{A}}^{\mathrm{Brown}} \tag{S7}$$

where $\dot{\mathbf{A}}^{\mathrm{J}}$ denoted the Jeffery term [10], $\dot{\mathbf{A}}^{\mathrm{FT}}$ denoted the FT term [11], $\dot{\mathbf{A}}^{\mathrm{Brown}}$ denoted

the Brownian motion term, which was introduced by Doi and Edwards [1] (see Eq. 8.127 and Eq. 8.149 in the their book). $\dot{\mathbf{A}}^{\mathrm{Brown}}$ was written as:

$$\dot{\mathbf{A}}^{\mathrm{Brown}} = 2D_r(\mathbf{I} - \mathbf{3A}) \tag{S8}$$

The rotational diffusion coefficient D_r becomes smaller for the semi-dilute suspensions ($a_r{}^{-2} \ll \varphi \ll a_r{}^{-1}$), and Doi and Edwards [1] estimated it to be $D_r = D_{r0}(a/L)^2$, where a the effective tube of fiber and D_{r0} is the rotational diffusion coefficient of dilute fiber suspensions. Here, D_{r0} was adopted in the calculation of the maximum influence of the Brownian motion for semi-dilute suspensions.

The diffusion coefficient D_{r0} was dependent on the size of the nanoparticles, and can be estimated by the shish-kebab model, as described in the book of Doi and Edwards (Eq. 8.16) [1]:

$$D_{r0} = \frac{3\,k_B T \ln(a_r)}{\pi \eta_s L^3} \tag{S9}$$

where k_B is the Boltzmann constant, $\eta_s = 330$ Pa·s is the viscosity of the polymer matrix, $\mathrm{L} = 219$ μm is the length of the fiber, $a_r = L/d$ is the aspect ratio of the fiber. The diameter of the glass fiber is $d = 18.4\,\mu\mathrm{m}$. Thus, D_{r0} was adopted as $D_{r0} = 4.1 * 10^{-12}\ \mathrm{s}^{-1}$ in these experiments.

Assuming that the initial state of the fibers was randomly orientated before pre-shear, the figure below plots the evolution of the components of orientation tensor $\mathbf{A}$ under pre-shear, where the fiber interaction parameter parameter C_I for 50 wt% (26.3 vol%) GF/PEB were calculated to be $C_I = 0.0269$ according to Eq. S6. The Brownian may induce significant changes in the fiber orientation by resting for 10^{10} s, which is much longer than our experiment time.

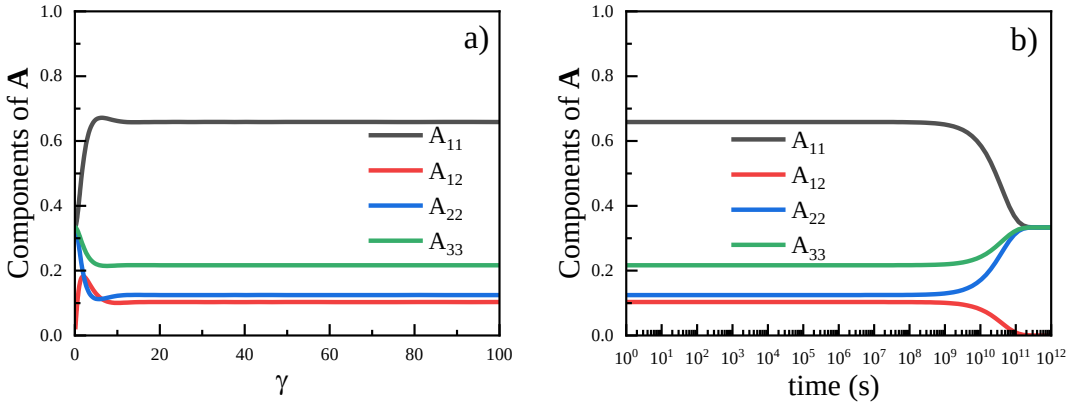

Figure S2. Evolution of the components of tensor **A** under shear predicted by FT+Brownian model a) and during rest b) predicted by the FT model where the fiber interaction parameter $C_I = 0.0269$ was calculated by Eq. S6. Evolution of the components of tensor **A** induced by Brownian motion during the resting step after preshear, with the rotational diffusion coefficient $D_r = 4.1 * 10^{-16}\ s^{-1}$.

6. Evolution of Shear Banding Boundary

We define a critical position y_c that separates the high-shear region and the low-shear region. The evolution of the normalized critical position y_c/H versus reversal shear strain γ is plotted in Fig. S3 for different suspensions. The evolution of y_c is more relevant to the fiber suspension instead of the confining condition. For 30 wt% fiber suspension, y_c often starts near the moving plates and evolves towards the stationary plate with propagating waves. The moving of the banding boundary is significant and requires a large strain to reach a steady position for 30 wt% suspension. The evolution of the banding boundary becomes less significant as fiber concentration increases. In 50 wt% suspension, y_c is almost a constant. In all cases, the steady position of the boundary of high and low shear regions is $y_c/H \approx 0.5$. Shear banding fluctuations could also be observed in dense granular materials under shear [13], which could be attributed to the particle migration from the local jamming regions (near the edge of the geometry) [14]. This migration continues until the pressures balance and the flow is no longer unstable. Then the system is unjammed, leading to the flow of local jamming regions and forming of new jamming regions elsewhere [14], which introduces solid-fraction waves across the samples [13]. However, the migration of glass fibers was strongly depressed in our experiments due to the much higher polymer matrix.

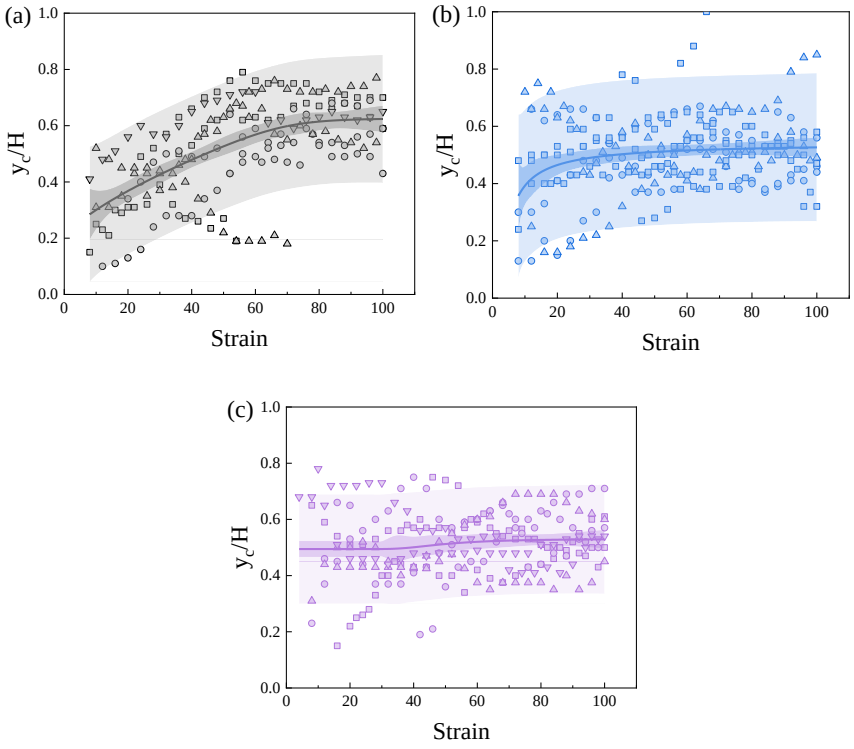

Figure S3. Evolution of the normalized critical position y_c/H that separates the low-shear and high-shear banding regions versus shear strain γ during reversal shear for (a) 30 wt%, (b) 40 wt%, and (c) 50 wt% PEB/GF composites. The applied shear stresses σ ranges from 300 Pa to 2400 Pa, and the gaps between the parallel plates were chosen as 0.5 mm, 1.0 mm, and 2.0 mm. Different symbols represent different shear stresses and gaps. The solid lines are the fitting curves of the logistic function.

7. Typical Velocity Profiles Using Cone-Plate

We made the sample into a donut shape (inner radius of 20 mm and outer radius of 30 mm) and put them into the cone-disc plates geometries (30 mm diameter with a cone angle of 0.1 rad). The velocity profiles of the cone-disc plates with donut-shaped sample are shown in the figure below. It also shows the "three-banding" behavior, consistent with the observations using parallel plates.

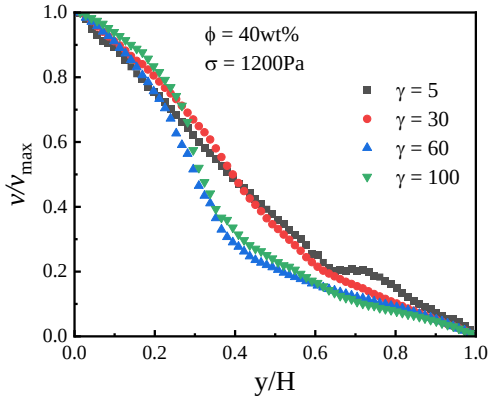

Figure S4. Velocity Profiles, normalized velocity $v/v_{\max}$ versus normalized position y/H during reversal shear. The sample, 40 wt% GF/PEB, was made into a donut shape with an inner diameter of 20 mm and outer diameter of 30 mm, and was sandwiched into cone-disc geometry (diameter of 30 mm with a cone angle of 0.1 rad). The shear stress is $\sigma = 1200$ Pa.

8. Wall Slip Behavior

Fig. S5 shows the typical velocity profiles of 50 wt% GF/PEB under different stresses, which shows that the velocity close 0 near the stationary plate while close to the plate velocity near the moving plate. It indicates that the wall slip is absent.

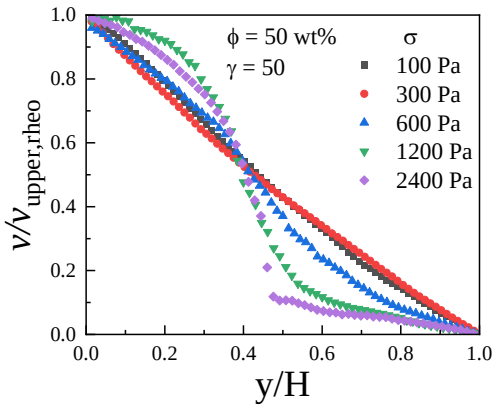

Figure S5. Normalized velocity profiles ($v/v_{\text{upper,rheo}} \sim y/H$) of 50 wt% GF/PEB under shear stresses ranging from $\sigma = 100$ Pa to 2400 Pa, where $v_{\text{upper,rheo}}$ is the vecolity of the upper plates calculated from the rheometer data. The gap H = 1 mm, the shear strain $\gamma = 50$.

9. Orientation Distribution for As-prepared and for $\gamma = 0$ and 1

Fig. S6 show the 3D XCT photo and **A** components of 50wt% as-prepared GF/PEB, which were hot-pressed into 1mm plates.

Fig. S7 and Fig. S8 show the 3D XCT photo of 50wt% GF/PEB after preshear shear (or $\gamma = 0$) and after reversal shear for $\gamma = 1$, where the gap is 1 mm.

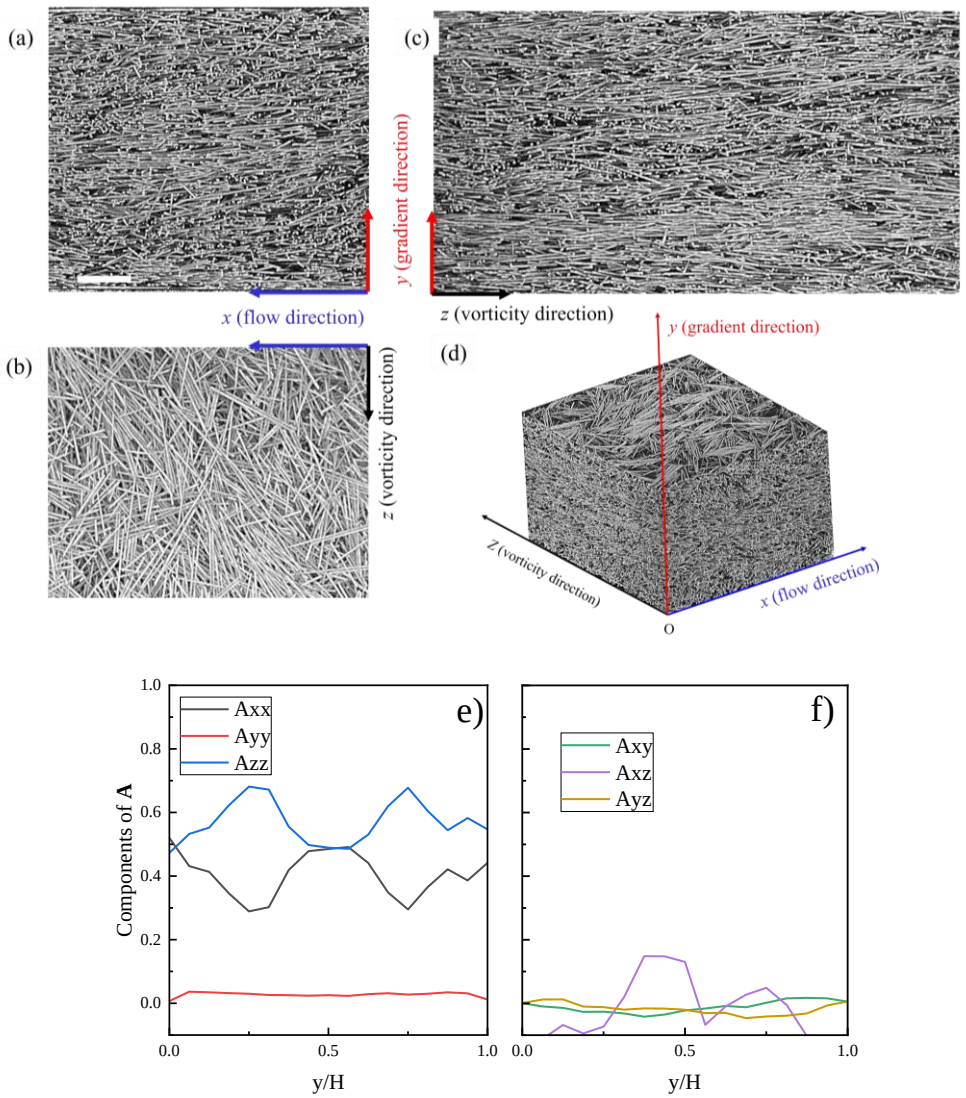

Figure S6. (a-d) 3D XCT photo of 50wt% as-prepared GF/PEB, which were hot-pressed into 1mm plates. (e-f) Components of orientation tensor A ($A_{xx}, A_{yy}, A_{zz}, A_{xy}, A_{xz}, A_{yz}$).

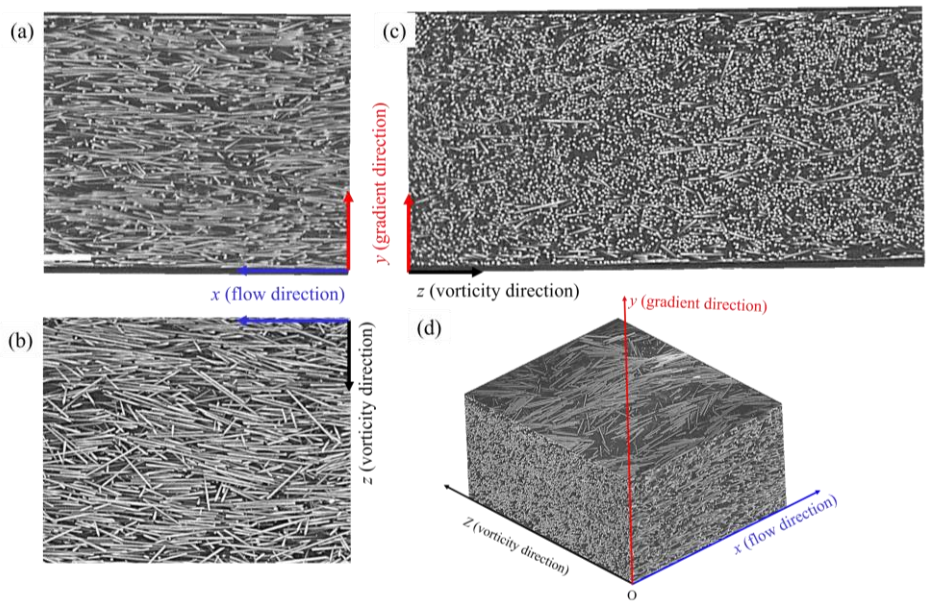

Figure S7. 3D XCT photo of 50wt% GF/PEB after the preshear process (or $\gamma = 0$), where the samples were sheared under a stress of 300 Pa for 100 units of strain. The scale bar is 200 μm.

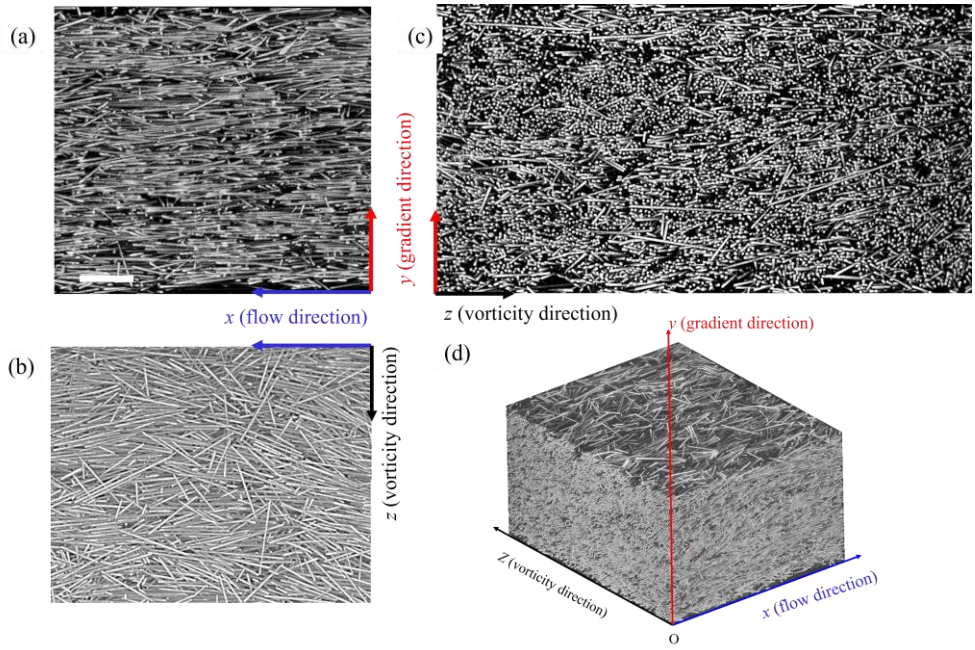

Figure S8. 3D XCT photo for 50wt% GF/PEB after reversal shear for $\gamma = 1$ under a shear stress of 1200 Pa.

10. Fiber Tumbling Predicted by the FT Model

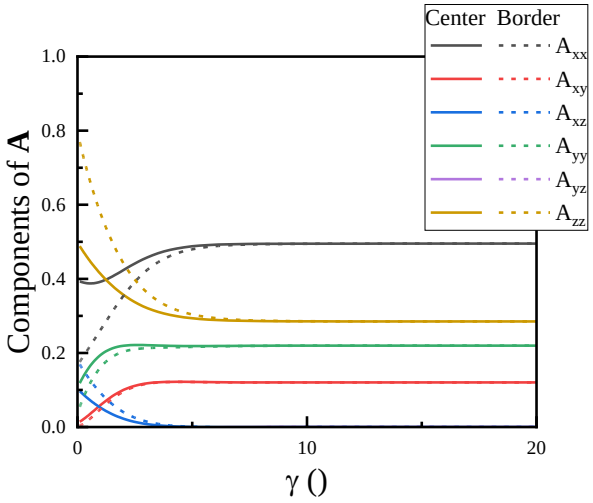

Figure S9. The evolution of orientation tensor A predicted by the FT model. The initial orientation state $\mathbf{A}_0$ was measured by CT, see Fig. 7-8 in the manuscript. The initial $\mathbf{A}_0$ is different from center of the gap to near the border of the gap.

11. Stress Growth with Zero Normal Force

50 wt% GF/PEB with a diameter of 25 mm and thickness of 1 mm were placed in the parallel plates of the Ares-G2 Rotational Rheometer. The samples were first sheared under a shear rate of 0.5 s^{-1} for 100 units of strain, and then reversal sheared under a shear rate of 1.0 s^{-1}, during which the normal stress was set as zero and left the gap changes. The results are shown in Figure S10, where the gap changes during the reversal shear, indicating the dilation effect of the concentrated glass fibers during the reversal shear.

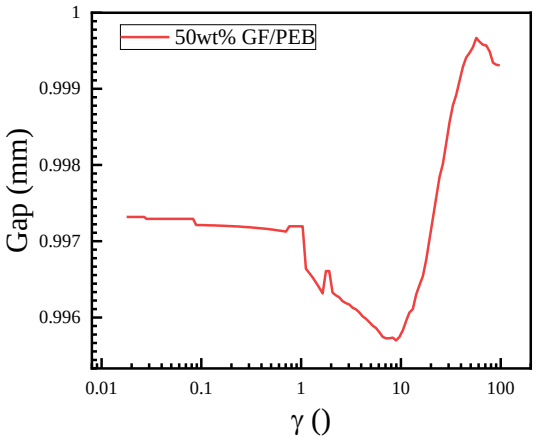

Figure S10. The gap versus strain of 50wt% GF/PEB composites during reversal shear when the normal force was adjusted to be zero and left the gap changes. The reversal shear rate is 1 s^{-1}.

References:

1. M. Doi and S. F. Edwards, *The theory of polymer dynamics*, Oxford University Press, 1988.
2. N. Quennouz, M. Shelley, O. du Roure and A. Lindner, *Journal of Fluid Mechanics*, 2015, **769**, 387-402.
3. L. E. Becker and M. J. Shelley, *Physical Review Letters*, 2001, **87**, 198301.
4. S. N. Bounoua, P. Kuzhir and E. Lemaire, *Journal of Rheology*, 2019, **63**, 785-798.
5. S. G. Advani and C. L. Tucker, *Journal of Rheology*, 1987, **31**, 751-784.
6. D. H. Chung and T. H. Kwon, *Journal of Rheology*, 2002, **46**, 169-194.
7. J. S. Cintra Jr and C. L. Tucker Iii, *Journal of Rheology*, 1995, **39**, 1095-1122.
8. G. B. Jeffery, *Proc. R. Soc. Lond. A*, 1922, **102**, 161-179.
9. D. Zhang, D. E. Smith, D. A. Jack and S. Montgomery-Smith, *Journal of Manufacturing Science and Engineering*, 2011, **133**.
10. F. Folgar and C. L. Tucker, *Journal of Reinforced Plastics and Composites*, 1984, **3**, 98-119.
11. N. Phan-Thien, X. J. Fan, R. I. Tanner and R. Zheng, *Journal of Non-Newtonian Fluid Mechanics*, 2002, **103**, 251-260.
12. B. Li, Y. Guo, P. Steeman, M. Bulters and W. Yu, *Journal of Rheology*, 2021, **65**, 1169-1185.
13. G. Ovarlez, A. Vu Nguyen Le, W. J. Smit, A. Fall, R. Mari, G. Chatté and A. Colin, *Science Advances*, 2020, **6**, eaay5589.
14. M. Hermes, B. M. Guy, W. C. K. Poon, G. Poy, M. E. Cates and M. Wyart, *Journal of Rheology*, 2016, **60**, 905-916.